An upper bound on the electrical conductivity of hydrated oceanic mantle at the onset of dehydration melting

Samer Naif

Lamont-Doherty Earth Observatory, Columbia University, Palisades, NY 10964, USA.

Abstract

Electrical conductivity soundings provide important constraints on the thermal and hydration state of the mantle. Recent seafloor magnetotelluric surveys have imaged the electrical conductivity structure of the oceanic upper mantle over a variety of plate ages. All regions show high conductivity (0.02 to 0.2 S/m) at 50 to 150 km depths that cannot be explained with a subsolidus dry mantle regime without unrealistic temperature gradients. Instead, the conductivity observations require either a small amount of water stored in nominally anhydrous minerals or the presence of interconnected partial melts. This ambiguity leads to dramatically different interpretations on the origin of the asthenosphere. Here, I apply the damp peridotite solidus together with plate cooling models to determine the amount of H_2O needed to induce dehydration melting as a function of depth and plate age. Then, I use the temperature and water content estimates to calculate the electrical conductivity of the oceanic mantle with a two-phase mixture of olivine and pyroxene from several competing empirical conductivity models. This

Email address: snaif@ldeo.columbia.edu ()

represents the maximum potential conductivity of sub-solidus oceanic mantle at the limit of hydration. The results show that partial melt is required to explain the subset of the high conductivity observations beneath young seafloor, irrespective of which empirical model is applied. In contrast, the end-member empirical models predict either nearly dry (<20 wt ppm H_2O) or slightly damp (<200 wt ppm H_2O) asthenosphere for observations of mature seafloor. Since the former estimate is too dry compared with geochemical constraints from mid-ocean ridge basalts, this suggests the effect of water on mantle conductivity is less pronounced than currently predicted by the conductive end-member empirical model.

Keywords: electrical conductivity, magnetotellurics, mantle hydration, origin of the oceanic asthenosphere, lithosphere-asthenosphere boundary

1. Introduction

The upper mantle is composed of rigid lithospheric plates that slide on ductile asthenosphere. The depth interval over which the rheological transition from rigid to ductile behavior occurs is known as the lithosphere-asthenosphere boundary (LAB). The mechanism responsible for the viscosity reduction at the LAB is often attributed to temperature, mineral hydration, or partial melting (Anderson and Sammis, 1970; Karato and Jung, 1998; Stixrude and Lithgow-Bertelloni, 2005; Faul and Jackson, 2005). Geophysical observations sensitive to all three mechanisms provide constraints on the origin of the LAB and the asthenosphere.

Magnetotelluric (MT) and seismic studies of oceanic plates both show contrasting material properties above and below the LAB. The lithosphere

often exhibits high seismic velocity and low electrical conductivity, while the asthenosphere exhibits low seismic velocity, strong seismic anisotropy, and high electrical conductivity (Kawakatsu and Utada, 2017). Seismic studies have identified a sharp velocity reduction below oceanic plates at depths thought to coincide with the LAB. Regions characterized by a sharp LAB typically experience a 5–10% shear wave velocity reduction over a depth interval less than 30 km thick, requiring unrealistic temperature gradients that are inconsistent with a thermal origin (Fischer et al., 2010). Although a thermal origin alone is less likely, debate persists over which mechanism, partial melting or mineral hydration, best explains the geophysical observations (Beghein et al., 2014).

Here, I focus on the electrical conductivity signature of the LAB beneath oceanic plates. The conductivity structure of the oceanic upper mantle has been observed by a relatively limited number of independent marine MT studies, each located in a unique tectonic setting. Since mantle conductivity varies as a function of temperature, water content, and partial melt fraction, MT data provide unique constraints on the origin of the asthenosphere (Yoshino and Katsura, 2013; Kawakatsu and Utada, 2017).

Most studies consider olivine as a proxy for the electrical properties of the bulk upper mantle since it is the primary mineral phase in peridotite (~60%) and laboratory measurements on dry olivine, pyroxene, and garnet show similar conductivity behavior (Xu and Shankland, 1999). Generally, the asthenosphere is 10^{-2} to 10^{-1} S/m. As is the case with seismic observations, this range of asthenospheric conductivity values also requires unrealistic temperatures for dry mantle olivine. Several independent laboratory studies have

reported distinct empirical models for the electrical conductivity of hydrous olivine (Gardés et al., 2014). The model discrepancies have led to conflicting interpretations of either hydration or partial melting as the cause of the electrical asthenosphere (Wang et al., 2006; Yoshino et al., 2006).

A global approach that assumes the mantle conductivity is controlled by olivine, however, masks the heterogeneity among MT studies, ignores the role of pyroxenes, and precludes considering the thermodynamic stability of a multiphase sub-solidus mantle in a regional context. Furthermore, due to the prominent effect of CO_2 on the solidus, recent studies suggest sub-solidus LAB is unable to explain conductivity observations for hydrous carbonated source mantle regardless of plate age, whereby incipient melts may be a ubiquitous feature of the LAB (e.g., Katsura et al., 2017). Since the gravitationally stability of incipient volatile-rich melts remains an open question, there is an inherent non-uniqueness when inferring hydration or partial melt from MT observations. Here, I demonstrate that when temperature and hydration are parameterized in a thermodynamically consistent framework and the mantle is treated as a two-phase mixture of olivine and pyroxene, none of the existing empirical conductivity models for hydrated mantle minerals can explain the high conductivity signature at LAB depths in MT observations made on young seafloor. Therefore, partial melting is the only viable mechanism to explain highly conductive LAB. By ignoring the role of CO_2, the present study clarifies when hydration is not a viable mechanism to account for the observed mantle conductivity and, in such cases, resolves the previously noted issue of non-uniqueness.

2. Mantle conductivity

2.1. Conduction in nominally anhydrous minerals

Peridotite rock is the primary constituent of the upper mantle and is made up of the nominally anhydrous minerals (NAMs) olivine, pyroxene, and garnet. In the absence of well-connected conductive phases such as metal oxides or fluids/melts, the electrical conductivity signature of the upper mantle is controlled by the concentration and diffusion of point defects through the crystal lattice structure of silicate minerals, both of which are thermally-activated processes (Yoshino and Katsura, 2013). Therefore, the conductivity behavior of mantle minerals can be described by empirical fitting of experimental conductivity data to an Arrhenius relation.

The dominant conduction mechanism for dry olivine is a combination of small polaron hopping (charge exchange between ferrous and ferric iron) and diffusion of magnesium vacancies (Schock et al., 1989)

$$\sigma_{dry} = A_{vac} \exp\left(\frac{-\Delta H_{vac}}{RT}\right) + A_{pol} \exp\left(\frac{-\Delta H_{pol}}{RT}\right) \tag{1}$$

where σ_{dry} is the anhydrous olivine conductivity, A_{vac} and A_{pol} are preexponential factors, ΔH_{vac} and ΔH_{pol} are activation enthalpies, R is the gas constant, and T is absolute temperature. In addition to temperature, mantle conductivity varies as a function of oxygen fugacity, iron content, and (to a lesser extent) pressure due to changes in defect concentration. For a quartz-fayalite-magnetite oxygen fugacity buffer representative of upper mantle conditions, dry olivine conductivity increases from approximately 10^{-6} S/m at 700°C to 10^{-2} S/m at 1400°C (Constable, 2006).

2.2. Hydrogen conduction

The electrical conductivity of the upper mantle is also dependent on the concentration of hydrogen defects (commonly referred to as water content) in NAMs due to the high chemical mobility of hydrogen that is incorporated as a charged species (H^+) (Karato, 1990). Experimental studies have confirmed that hydrated NAMs are significantly more conductive than their dry counterpart. However, there are significant inter-study disagreements regarding the degree to which water enhances conductivity (Gardés et al., 2014). Furthermore, it is not yet clear which hydrogen conduction mechanism is responsible for the enhancement and whether a single or multiple species of hydrogen are operating (Du Frane and Tyburczy, 2012; Karato, 2013).

The conduction mechanism for hydrated NAMs has been expressed in one of two forms. Wang et al. (2006) developed an Arrhenian relation for olivine conductivity that takes into account hydrogen speciation

$$\sigma_{wet} = A_{wet} C_w^r \exp\left(\frac{-\Delta H_{wet}}{RT}\right) \tag{2}$$

where C_w is the water content and exponent r is a constant. For $r = 1$ all of the hydrogen contributes equally to conduction and when r is less than one it implies the concentration of hydrogen that influences conductivity is some fraction of the total concentration. Yoshino et al. (2009) proposed an alternative relation that treats hydrogen as a single species

$$\sigma_{wet} = A_{wet} C_w \exp\left(\frac{-\Delta H_{wet} - \alpha C_w^{1/3}}{RT}\right) \tag{3}$$

where α is a constant. The exponent r, which is not included in the equation, is implicitly assumed to equal unity, such that all of the incorporated

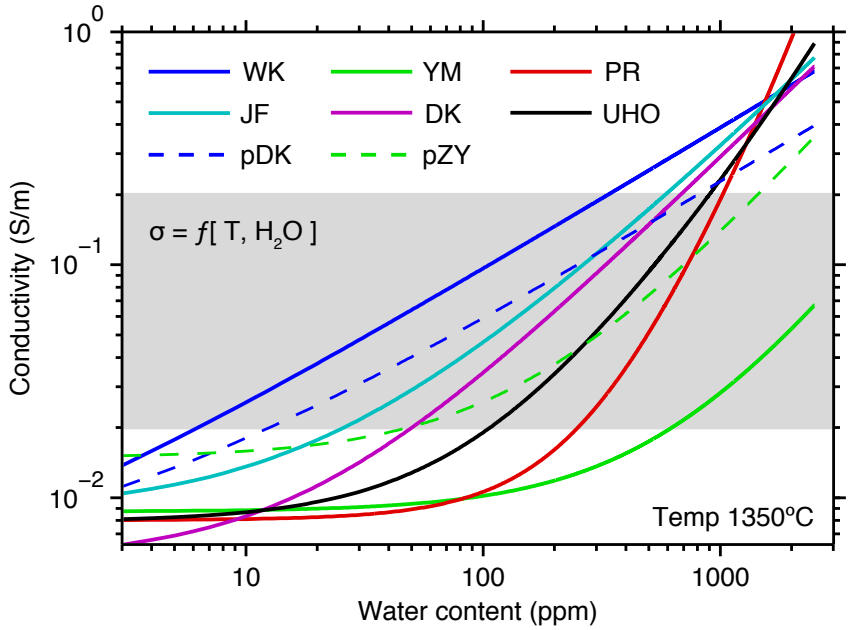

Figure 1: Comparison of six hydrous olivine and two hydrous pyroxene conductivity laws. Solid and dashed lines show predicted electrical conductivity of olivine and pyroxene as a function of water concentration at 1350°C, respectively. Predictions vary by up to one order of magnitude. The shaded region represents the typical range of observed asthenosphere conductivity. WK = Wang et al. (2006). YM = Yoshino et al. (2009). PR = Poe et al. (2010). JF = Jones et al. (2012). DK = Dai and Karato (2014). UHO = Gardés et al. (2014). pDK = Dai and Karato (2009). pZY = Zhang et al. (2012).

hydrogen contributes equally to the conductivity. The α and C_w terms were included in the exponential function to account for the water concentration dependence of the activation energy seen in their experimental data. This has the net effect of increasing the contribution of hydrogen conduction to the bulk conductivity at higher water concentrations.

Figure 1 shows a comparison of several existing hydrous conductivity models for olivine and pyroxene at 1350°C. Since conductivity experiments

on hydrous NAM samples are prone to dehydration at high temperatures (>1000°C), the trends are extrapolations of lower temperature measurements to asthenospheric conditions. The WK (Wang et al., 2006), DK (Dai and Karato, 2014), and pDK (Dai and Karato, 2009) models adopted the Arrhenian relation in equation 2. The YM (Yoshino et al., 2009), PR (Poe et al., 2010), UHO (Gardés et al., 2014), and pZY (Zhang et al., 2012) models used the relation in equation 3. The JF model (Jones et al., 2012) used a hybrid of both relations, in which the exponent term r was included in equation 3 and explicitly allowed to vary. Supplementary Table S1 lists the parameter values for all of the empirical models shown in Figure 1.

Some of the conductivity studies were performed on single crystals and reported a unique empirical fit for each crystallographic orientation. Although the experiments provided an additional constraint on the electrical anisotropy, a comparison of the results also shows significant disagreements (Poe et al., 2010; Yang, 2012; Dai and Karato, 2014). Since the scope of this paper is limited to isotropic conductivity, the single crystal experiments that reported parametric fits to individual axes were geometrically averaged in all three directions to give an isotropic form of the law: $\sigma_{iso} = (\sigma_{[100]}\sigma_{[010]}\sigma_{[001]})^{1/3}$.

2.3. Hydrous olivine conductivity discrepancies

The first two laboratory studies to quantify the effect of water on olivine conductivity were performed by independent groups and published simultaneously, yet reported distinct measurements that differed by an order of magnitude (Yoshino et al., 2006; Wang et al., 2006). Such a large discrepancy led to conflicting interpretations on the origin of the asthenosphere;

Wang et al. (2006) inferred hydration while Yoshino et al. (2006) inferred partial melt as the responsible mechanism. As can be seen in Figure 1, more recent experimental studies have also reported distinct measurements and proposed unique Arrhenian conductivity models specific to the data of each study (Yoshino et al., 2009; Poe et al., 2010; Dai and Karato, 2014).

The source of the experimental discrepancies could be attributed to a number of complicating factors. In an effort to quantify the experimental uncertainties, Gardés et al. (2014) compiled a database of all existing hydrous olivine conductivity measurements at the time and proposed that inter-laboratory disagreements likely stem from errors in the water content estimates. Poe et al. (2010) noted that previous workers used non-polarized Fourier Transform Infrared Spectroscopy (FTIR) with the Paterson (1982) calibration to measure the water content in olivine samples. For anisotropic minerals such as olivine, both the Paterson (1982) calibration, which was determined from the spectra of water in glass and quartz, and non-polarized IR radiation could lead to large systematic biases in water content measurements. Indeed, olivine specific polarized FTIR calibrations demonstrate that the Paterson (1982) calibration underestimates water contents by a factor of about 2.3 in natural and 1.7 in synthetic olivine samples (Bell et al., 2003; Mosenfelder et al., 2006; Withers et al., 2012). Bell et al. (2003) also reported that using non-polarized spectra with the Paterson (1982) calibration underestimated water in their natural olivine samples by a factor of 3.5. However, the conversion factors are only applicable to the set of samples considered by a particular study; there is no universal conversion to correct for the water concentration of other olivine samples measured with non-polarized FTIR

(Libowitzky and Rossman, 1996; Bell et al., 2003; Withers et al., 2012).

In lieu of applying a potentially inaccurate correction to the reported water contents of experimental data, Gardés et al. (2014) increased the upper bound limit of uncertainty by a factor of 3.5 for polycrystalline samples and used regression analysis to find the best fitting "Universal Hydrous Olivine" (UHO) conductivity model for the compiled dataset (although the data of Yoshino et al. (2009) were excluded). The UHO model is consistent with the largest fraction of existing experimental data. At 100 wt ppm H_2O and 1350°C, the UHO conductivity estimates sit approximately halfway between those of the PR and DK models.

Without independent confirmation that the water contents estimated from non-polarized FTIR measurements are biased – specifically for the samples used in conductivity experiments – it is yet to be determined which of the empirical hydrous olivine conductivity models most accurately represents the oceanic upper mantle.

3. Mantle H_2O storage capacity

Water drastically reduces the melting temperature of mantle minerals. While it might otherwise be possible to explain mantle conductivity observations with a geochemically reasonable concentration of water, this does not guarantee thermodynamic stability of sub-solidus mantle. Indeed, the upper mantle beneath young oceanic plates is warm enough to induce melting even under dry conditions. In order to determine the thermodynamically viable mechanism (partial melting or hydration) that explains observations of mantle conductivity, it is necessary to quantify how much water the mantle can

hold before crossing the solidus and undergoing dehydration melting.

For a given depth and temperature, the solidus of hydrated mantle can be used to back out the water concentration (i.e., H_2O storage capacity) that is required at the onset of dehydration melting. I assign temperature, T_{plate}, as a function of depth and plate age from two plate cooling models: the Hasterok (2013) model with 90 km plate thickness and 1350°C mantle potential temperature (MPT) and the Stein and Stein (1992) model with 95 km plate thickness and 1420°C MPT. Using two models with different MPTs helps to quantify the effect of temperature on the H_2O storage capacity, and thus their compounding effect on electrical conductivity. Below the base of the plate, temperature is independent of plate age and increases adiabatically with depth. Both geotherms include an adiabatic gradient of 0.3°C/km.

The damp solidus is commonly estimated relative to the dry melting temperature. For a typical peridotite composition, Hirschmann (2000) found the dry solidus to be

$$T_{dry} = -5.141P^2 + 132.899P + 1393.811 \tag{4}$$

where T_{dry} is the dry melting temperature in kelvin and P is pressure in gigapascal. Here, I adopt the parametrization of Hirschmann et al. (2009), but substitute the updated pyroxene partition coefficients from O'Leary et al. (2010), to estimate the hydrous peridotite solidus with the cryoscopic approximation

$$T_{wet} = \frac{T_{dry} + T_{cor}}{\left(1 - \left(R/\Delta\hat{S}_{fusion}\right)\ln\left(1 - X_{OH^-}^{melt}\right)\right)} \tag{5}$$

where T_{wet} is the hydrated peridotite solidus, T_{cor} is a user prescribed constant that shifts the dry solidus to a higher or lower temperature, R is the

gas constant, $\hat{S}_{fusion}$ is the molar entropy of fusion, and $X_{OH^-}^{melt}$ is the mole fraction of hydroxyl in the partial melt. The purpose of T_{cor} is to accommodate a temperature correction for the dry solidus. According to a recent study that experimentally quantified the solidus of damp peridotite at low water concentrations (Sarafian et al., 2017), the dry solidus in equation 4 underestimates the melting temperature by 60°C (hence $T_{cor} = 60$).

The cryoscopic approach depends on the mantle composition as well as the H_2O partition coefficients between minerals and melts, both of which are factored into the calculation of the hydroxyl mole fraction ($X_{OH^-}^{melt}$) in the partial melt. The value of $X_{OH^-}^{melt}$ also depends on the molar unit of mass that is applied. Hirschmann et al. (2009) found that using an oxide molar unit (59 g/mol) provides a good fit to the freezing-point depression for experimental data with melt water concentrations of less than 4.5 wt% H_2O, but overestimates it at higher concentrations (see their Fig. 9). I assign a molar unit of 180 g/mol, which gives an improved fit to the few available data at high water concentrations. In the cryoscopic approximation, a larger molar mass reduces the effect of water on the solidus and thus increases the H_2O storage capacity.

Having estimated temperature as a function of plate age and depth ($T_{plate} = f[z, t]$) and the damp solidus as a function of water content and depth ($T_{wet} = f[z, H_2O]$), it is possible to calculate the H_2O storage capacity as a function of plate age and depth by determining the water concentration required to make $T_{wet} = T_{plate}$. The H_2O storage capacity determined here represents the highest water concentration that the mantle can hold without inducing dehydration melting and hence ignores water solubility in NAMs.

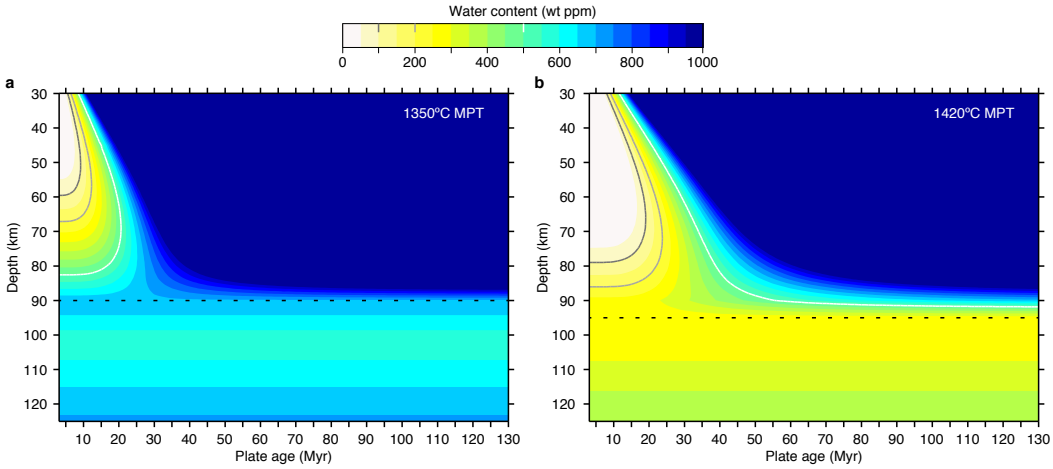

Figure 2: Water storage capacity as a function of plate age and depth for (a) 1350°C MPT plate cooling model (Hasterok, 2013) and (b) 1420°C MPT plate cooling model (Stein and Stein, 1992). Higher temperatures depress the storage capacity. The dark gray, light gray, and white lines represent the 100, 200, and 500 wt ppm H_2O contours. The dashed black lines show the plate thickness, below which temperature increases adiabatically.

Figure 2 shows the resulting storage capacity for both plate cooling models. As expected, the predicted storage capacity for the colder plate cooling model is larger since higher water concentrations are required to achieve additional reductions in the melting temperature. Since temperatures beneath the base of the plate are independent of plate age, the storage capacity there varies only with depth.

4. Results

4.1. Maximum conductivity of hydrated sub-solidus mantle

Now that the plate cooling models and damp peridotite solidi have been used to define a physically plausible range for the H_2O storage capacity, the

electrical conductivity (at the limit of hydration) is readily estimated from any of the empirical conductivity laws shown in Figure 1. To achieve a more accurate representation of the upper mantle, I calculate the bulk conductivity for a two-phase system consisting of olivine and pyroxene with the isotropic Hashin-Shtrikman upper bound (HS^+) mixing model

$$\sigma_{HS^+} = \sigma_{px} + (1 - \phi_{px}) \left(\frac{1}{\sigma_{ol} - \sigma_{px}} + \frac{\phi_{px}}{3\sigma_{px}} \right)^{-1} \tag{6}$$

where σ_{HS^+} is the bulk mantle conductivity, σ_{px} is the hydrous pyroxene conductivity, σ_{ol} is the hydrous olivine conductivity, and ϕ_{px} is the proportion of pyroxene. The volume proportion and water concentration of each mineral phase is adopted from Section 3 and shown in Figure S1. Since pyroxene holds around one order of magnitude more water than olivine, it is consistently more conductive than coexisting olivine regardless of the empirical model applied, and thus is assigned as the conducting phase in equation 6. Given that HS^+ assumes an isotropic spherically symmetric mixture where the primary phase is the body and the conducting phase is the shell, such a geometry likely overestimates the effect of pyroxene. More realistic isotropic geometries would yield lower bulk mantle conductivity estimates.

However, upper mantle peridotite is composed of four primary phases: olivine, orthopyroxene, clinopyroxene, and garnet. Existing hydrous clinopyroxene conductivity measurements on samples of peridotitic composition are significantly more resistive than olivine and orthopyroxene at low temperatures, but trend towards equivalent values at asthenospheric temperatures (Zhao and Yoshino, 2016). Given the similar conductivity behavior and magnitude of water held by both pyroxene phases, the two are combined and

treated as a single phase

$$C_{w,px} = \frac{\phi_{opx} C_{w,opx} + \phi_{cpx} C_{w,cpx}}{\phi_{opx} + \phi_{cpx}} \tag{7}$$

where subscript *cpx* is clinopyroxene and *opx* is orthopyroxene. When applied to equation 6, the pyroxene proportion $\phi_{px} = \phi_{opx} + \phi_{cpx}$.

Although garnet holds nearly twice the water in olivine, it likely has a second order effect on mantle conductivity due to its low proportion. Instead of ignoring garnet altogether, it is combined with the olivine phase in order to conserve the bulk upper mantle water content that will be used for estimating the conductivity

$$C_{w,ol} = \frac{\phi_{gt} C_{w,gt} + \phi_{ol} C_{w,ol}}{\phi_{gt} + \phi_{ol}} \tag{8}$$

where subscript *gt* is garnet and *ol* is olivine.

Of the 12 possible mixtures of olivine and pyroxene empirical conductivity models from Figure 1, I consider the least conductive combination given by YM with pZY and the most conductive combination given by WK with pDK. Each mixture is used to calculate the mantle conductivity with the two sets of thermal structure and storage capacity estimates derived from the colder and warmer plate cooling models, but with the maximum bulk water concentration capped at 500 wt ppm H_2O. Figure 3 shows the four mantle conductivity predictions as a function of plate age and depth.

At depths shallower than the plate thickness, all of the predictions initially experience a rise in conductivity with increasing plate age due to increasing water storage capacity. The conductivity peaks where the storage capacity reaches its pre-defined maximum value and begins to fall with increasing age

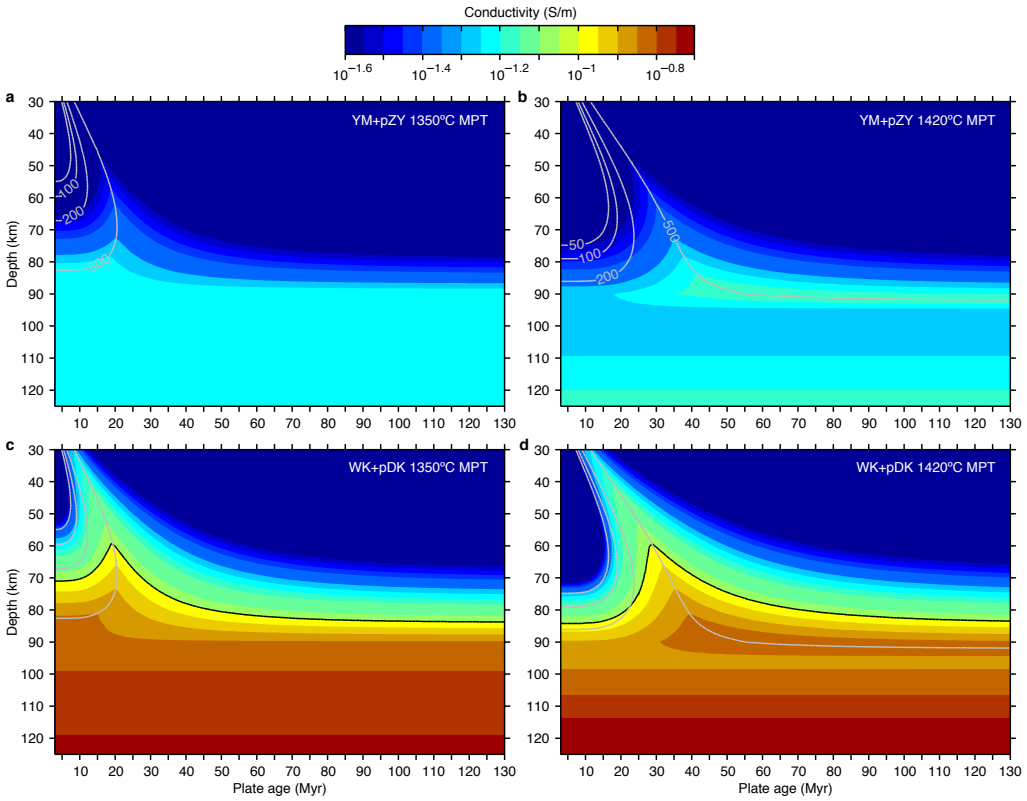

Figure 3: Maximum electrical conductivity of hydrated mantle as a function of plate age and depth calculated with the following conductivity and plate cooling models: (a) YM+pZY and 1350°C MPT, (b) YM+pZY and 1420°C MPT, (c) WK+pDK and 1350°C MPT, (d) WK+pDK and 1420°C MPT. Storage capacity capped at 500 wt ppm H_2O. Black line is the 0.1 S/m contour, and gray lines are the 50, 100, 200, and 500 wt ppm H_2O contours from Figure 2.

since the water content remains constant while the plate temperature continues to cool. At depths greater than the plate thickness, the conductivity is insensitive to age since both the temperature and storage capacity vary only with depth.

The estimates from the warmer plate cooling model (1420°C MPT) show a zone of depressed conductivity at about 90–100 km depths. There are two sources for the inverted conductivity gradient near those depths. The first source is related to a sudden change in mantle composition at the onset of garnet stability. Between 2.8 GPa (90 km) and 3.2 GPa (102 km), the proportion of garnet in the mantle increases from 0% to 13.5% while orthopyroxene decreases from 28% to 14%. As previously noted, garnet is less conductive than the pyroxene it replaces since it holds about five to ten times less water. Therefore, the swap in mineral proportions sharply reduces ϕ_{px} in equation 6 and has the net effect of lowering the bulk mantle conductivity estimates at 90–100 km depths. The second source, which has less of an impact on the conductivity, is produced by a progressive reduction in the water storage capacity of orthopyroxene at depths below 90 km due to decreasing Al_2O_3 concentrations (Mierdel et al., 2007; Hirschmann et al., 2009). These effects are muted in the conductivity estimates from the colder cooling model since the water storage capacity below the plate exceeds the 500 wt ppm H_2O cap applied here (see Fig. 2).

Figure 3 suggests that MT observations showing highly conductive mantle (~0.1 S/m) at LAB relevant depths (50–100 km) can be explained by hydration alone. Yet this requires water concentrations of up to 500 wt ppm H_2O, considerably higher than the 50–200 wt ppm H_2O observed in MORB

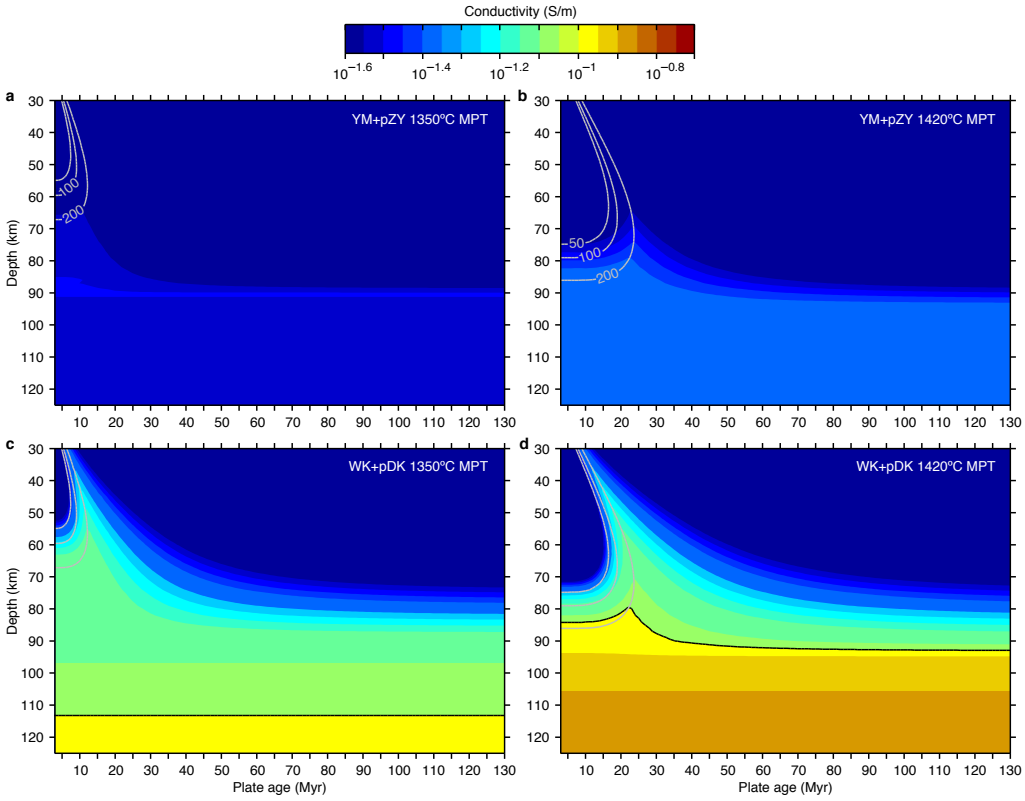

Figure 4: Maximum electrical conductivity of hydrated mantle as a function of plate age and depth. Storage capacity capped at 200 wt ppm H_2O. Black line is the 0.1 S/m contour, and gray lines are the 50, 100, and 200 wt ppm H_2O contours from Figure 2.

samples (Saal et al., 2002). Since such high water concentrations are unrealistic under "normal" mantle conditions, I recalculate the upper bound limit on conductivity with the storage capacity capped at 200 wt ppm H_2O. Figure 4 shows that these estimates are significantly less conductive. Therefore, a reasonable degree of hydration is not likely to account for highly conductive LAB in MT observations.

4.2. Application to MT observations

Existing marine MT studies span a wide range of seafloor ages and often image upper mantle conductivity values that require unrealistic temperatures for a dry mantle end-member. To assess whether hydration is sufficient to explain the conductivity constraints, I use the least conductive (YM+pZY) and most conductive (WK+pDK) mixtures applied in the predictions to estimate the degree of hydration needed to match the MT observations. If the hydration estimates exceed the H_2O storage capacity, then partial melt is the only plausible mechanism.

MT observations from the Serpentinite, Extension, and Regional Porosity Experiment across the Nicaragua Trench (SERPENT) and the Mantle Electromagnetic and Tomography (MELT) experiment both show anisotropic high conductivity channels at relatively shallow depths beneath young seafloor (Evans et al., 2005; Naif et al., 2013). Because the present study does not consider anisotropy and the exact amount of anisotropy seen in MT models is somewhat dependent on the prescribed inversion regularization (Baba et al., 2006), I convert the anisotropic models to an isotropic equivalent by geometrically averaging the conductivity along all three axes, $\sigma_{iso} = (\sigma_x \sigma_y \sigma_z)^{1/3}$. For clarity, I also simplify each of the 2D inversion models to a 1D conductivity-depth profile by determining the maximum conductivity observed laterally per unit depth. The lateral extent considered is 70–350 km distance from the ridge axis for the MELT inversion model and 200–300 km distance from the coastline for SERPENT.

The conductive channel observed in the MELT study area is located beneath 1.3–4.5 million years old (Ma) seafloor of the Nazca plate. In Figure

5a–c, the left panel shows the 1350°C and 1420°C MPT geotherms for 3 Ma seafloor, the middle panel shows the maximum observed isotropic conductivity, and the right panel shows the water concentration needed to match the observed conductivity. The isotropic conductivity reaches a peak of 0.047 S/m at 85 km depth. Note that the depth to the peak conductivity here is shallower than the peak at 100 km seen in Figure 3 of Evans et al. (2005) since the latter was determined from the horizontally averaged conductivity. Figure 5c shows that the water contents estimated with the warmer geotherm exceed the storage capacity and require a partial melt interpretation.

The conductive channel observed in the SERPENT study area, beneath the outer rise of 22–24 Ma Cocos plate seafloor, is significantly more conductive and reaches a peak of nearly 0.17 S/m at 55 km (Fig. 5e). In the case of 23 Ma plate, the predicted conductivity (from WK+pDK and 1420°C MPT) at 55 km depth is 0.084 S/m at the limit of hydration (325 wt ppm H_2O; Fig. 3d), or 0.063 S/m for 200 wt ppm H_2O (Fig. 4d). Since the water concentration estimates shown in Figure 5f all exceed the storage capacity, the only viable inference is partial melting. It is not clear what influence (if any) tectonic processes associated with the outer rise and subduction zone may have on the electrical signature of the LAB channel.

MT observations beneath mature seafloor should exhibit lower conductivity at lithospheric depths due to colder plate temperatures. Figure 6 shows the isotropic conductivity observations from two such studies: the NoMelt and Normal Oceanic Mantle (NOMan) experiments (Baba et al., 2013; Sarafian et al., 2015). The NoMelt survey, on 70 Ma Pacific plate seafloor, provides an example where the conductivity is most consistent with

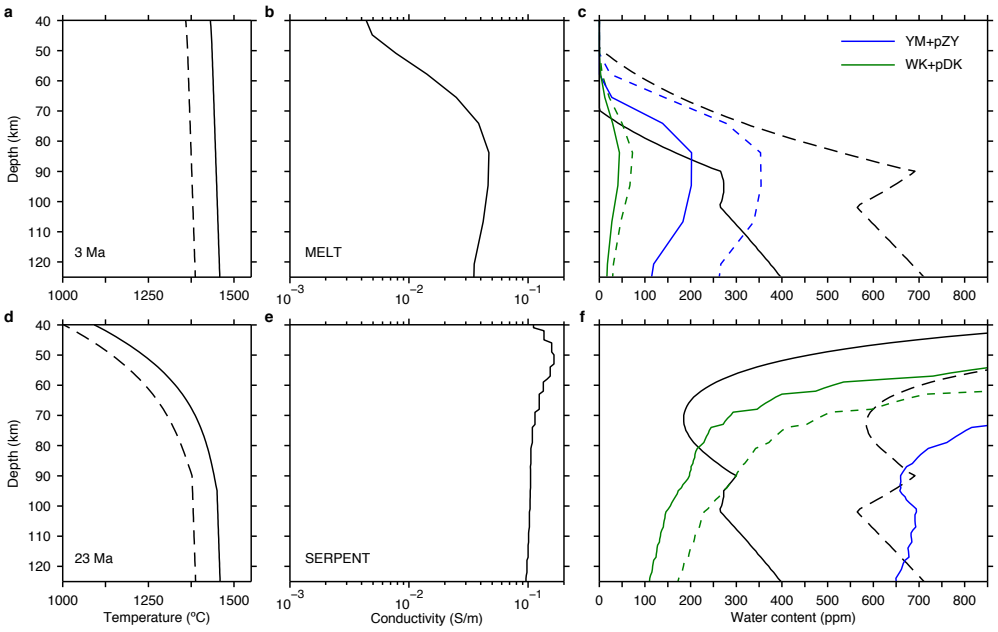

Figure 5: Water content inferred from MT observations on young seafloor. (a) 3 Ma geotherms. (b) Maximum observed isotropic conductivity from MELT survey. (c) Water storage capacity of 3 Ma plate for 1350°C MPT (dashed black line) and 1420°C MPT (solid black line) versus water content estimates needed to match the MELT MT observations. Dashed and solid lines show the water content estimates for the 1350°C and 1420°C MPT plate cooling models with the YM+pZY (blue) and WK+pDK (green) conductivity models, respectively. (d) 23 Ma geotherms. (e) Maximum observed isotropic conductivity from SERPENT survey. (f) Storage capacity of 23 Ma plate versus water content estimates needed to match the SERPENT MT observations (Legend same as Figure 5c).

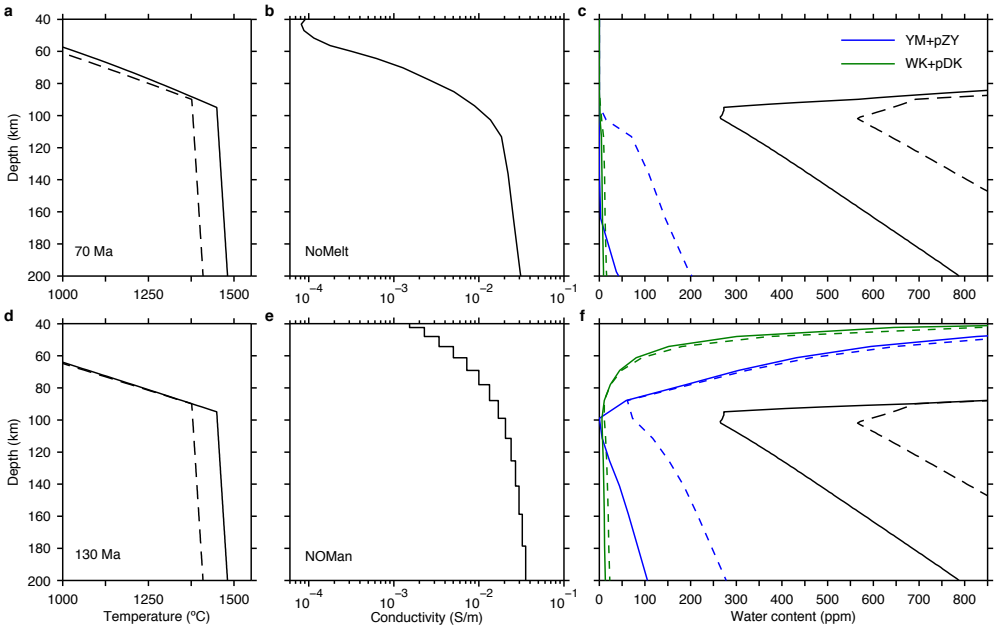

Figure 6: Water content inferred from MT observations on mature seafloor. Legend same as in Figure 5. (a) 70 Ma geotherms. (b) Maximum observed isotropic conductivity from NoMelt survey. (c) Water storage capacity of 70 Ma plate versus water content estimates needed to match the NoMelt MT observations. (d) 130 Ma geotherms. (e) Maximum observed isotropic conductivity from NOMan survey. (f) Storage capacity of 130 Ma plate versus water content estimates needed to match the NOMan MT observations.

a 100 km thick dry lithosphere sitting on nearly dry to slightly damp asthenosphere (less than 200 wt ppm H_2O).

The mantle conductivity from the NOMan survey, on 130 Ma Pacific plate seafloor, shows a similar trend to but is slightly more conductive than the NoMelt results for depths greater than 100 km. In the lithosphere, however, the NOMan conductivity decays at a considerably slower pace than predicted for dry olivine, so much so that the water concentrations needed to match the observations rapidly increase with decreasing depth. In order to explain the

conductivity within the lithosphere as dry mantle, the geotherm would need to resemble that of 16-20 Ma plate with 1420°C MPT. However, a relatively conductive lithosphere is a common trait in most MT observations since the data are known to lack sensitivity to the true conductivity value for resistive structures.

5. Discussion

5.1. Applicability of hydrous olivine conductivity models

Previous attempts to infer the degree of hydration from MT observations often assume the mantle is composed entirely of olivine. For the conductivity of olivine to be representative of the bulk peridotite mantle the water content and conductivity behavior of all coexisting NAMs must be equivalent. This is potentially problematic because pyroxenes, which constitute up to 40% of the upper mantle, may hold approximately 10 to 20 times more water than olivine at LAB relevant depths (Mierdel et al., 2007). Figure S2 shows the conductivity for an olivine-only mantle normalized by the two-component conductivity for an olivine-pyroxene mixture. The normalized conductivity trends deviate significantly from unity, which suggests pyroxenes cannot be ignored when interpreting upper mantle conductivity. At 100 km depth the YM (olivine) model is two (1350°C) to three (1420°C) times less conductive than YM+pZY, while the WK (olivine) model is 1.75 times more conductive than WK+pDK (for both MPTs).

Given that water preferentially partitions into the pyroxenes, it is important to note that using the HS^+ mixing model to estimate conductivity of a two-component mixture implies isotropic randomly distributed mineral

grains. For layered or sheared peridotite, the mineral distribution is less likely to be random. In that case, pyroxenes may be interconnected and could dominate the mantle conductivity signature (A. Pommier, personal communication, 2017) such that the HS^+ conductivity would not be representative of the bulk mantle.

5.2. Maximizing the water storage capacity

The aim of this study is to define an upper bound limit on the electrical conductivity of sub-solidus oceanic mantle. To achieve this, it is necessary to maximize the calculation of the mantle H_2O storage capacity. Shifting the melting temperature of dry peridotite to be 60°C warmer (based on the results of Sarafian et al. (2017)) and applying a molar mass of 180 g/mol (as opposed to 59 g/mol) both yield larger H_2O storage capacity estimates.

The 60°C correction included in the dry solidus has a large effect on the resulting conductivity predictions. Excluding the correction sharply reduces the H_2O storage capacity, which translates into a significant reduction in the upper bound limit on sub-solidus mantle conductivity. For example, the storage capacity at 100 km depth is increased from 327 to 583 wt ppm H_2O (1350°C MPT) and 89 to 268 wt ppm H_2O (1420°C MPT) when the correction is applied. This is equivalent to enhancing the YM+pZY and WK+pDK conductivity estimates from 0.043 to 0.071 S/m and 0.12 to 0.18 S/m at 1350°C MPT and from 0.031 to 0.053 S/m and 0.075 to 0.14 S/m at 1420°C MPT, respectively. By comparison, increasing the molar mass from 59 to 180 g/mol increases the storage capacity at 100 km depth from 429 to 583 wt ppm H_2O (1350°C MPT) and 227 to 268 wt ppm H_2O (1420°C MPT). This is equivalent to enhancing the YM+pZY and WK+pDK conductivity

estimates from 0.055 to 0.071 S/m and 0.15 to 0.18 S/m at 1350°C MPT and from 0.049 to 0.053 and 0.13 to 0.14 S/m at 1420°C MPT, respectively.

5.3. Effect of carbon-dioxide on the peridotite solidus

The hydrous mantle conductivity predictions only consider the effect of water on the solidus and ignore CO_2, which also produces a significant reduction in the melting temperature of peridotite (Dasgupta et al., 2013). In fact, the effect of carbon-dioxide on the solidus is so large that even trace amounts of CO_2 (<100 wt ppm) would induce melting at LAB depths regardless of plate age. Carbonated peridotite would yield very small melt fractions ($\ll$1%) yet this may be sufficient to explain most MT observations since carbonatite and hydrous carbonated silicate melts are up to two orders of magnitude more conductive than hydrous silicate melts (Sifré et al., 2014) and form gravitationally stable well-connected networks even at such low melt fractions (Holtzman, 2016). Although carbonatite melt may be unstable at LAB depths beneath oceanic plates younger than 40 Ma (Hirschmann, 2010), a plausible alternative is hydrous carbonated silicate melt. Given the latter case, it is difficult to distinguish between volatile-rich incipient melt and hydration with MT observations alone. The upper bound conductivity predictions for hydrous sub-solidus mantle presented here provide an important additional constraint.

5.4. Effect of ridge melting on plate hydration

The preceding discussion as well as the water storage capacity estimates described in Section 3 assume a static mantle and ignore the effect of melt transport and volatile extraction at mid-ocean ridges. Since water has a

strong affinity for partitioning into the liquid phase, the production and extraction of melt leaves behind a dry mantle residue. Therefore, MORB melting of upwelling mantle beneath the ridge axis is expected to generate a dehydration boundary in oceanic lithosphere, with dry mantle above and damp mantle below (Hirth and Kohlstedt, 1996).

The depth to the dehydration boundary is controlled by the onset of dry melting, and thus can be inferred from the dry peridotite solidus and the mantle potential temperature. For 1350°C MPT and 1420°C MPT (with 0.3°C/km adiabat), the oceanic lithosphere will be dry above 50 km and 70 km depths, respectively. Although not completely dry, a significant amount of water is also extracted at depths between the onset of dry and damp melting (Hirth and Kohlstedt, 1996). For mantle containing 200 wt ppm H_2O, damp melting initiates at 67 km and 86 km depth beneath the ridge for 1350°C MPT and 1420°C MPT, respectively. The volatile extraction would significantly reduce the upper bound conductivity predictions over the depth interval where MORB melting occurs. The water concentration and hence the conductivity of the oceanic upper mantle is unaffected by MORB processes at depths below the onset of damp melting.

5.5. Origin of the electrical LAB beneath oceanic plates

The four MT case studies described in Section 4.2 demonstrate that the stability of hydrated mantle in a sub-solidus thermal regime must be considered in a regional context when interpreting electrical conductivity observations. The SERPENT and NoMelt results are two end-member examples, where the former requires partial melt and the latter is consistent with dry lithosphere above nearly dry to damp asthenosphere. As previously noted,

while the NoMelt asthenosphere can be explained with hydration this does not rule out partial melting as an alternative interpretation (Sarafian et al., 2015).

The MELT results require partial melt for the warmer 1420°C MPT geotherm based on both the YM+pZY and WK+pDK conductivity predictions. The colder geotherm conductivity predictions yield water content estimates that do not exceed the H_2O storage capacity. However, at the ridge axis of the MELT study area, the MT and collocated seismic observations both support melting much deeper than 67 km (Forsyth et al., 1998; Baba et al., 2006). Therefore, either significantly higher volatile content or a MPT warmer than 1350°C is required to allow deeper melting (see discussion in Section 5.4). In light of these additional observational constraints, the only plausible interpretation for the conductive channel at depths shallower than 80–90 km is partial melt.

For NoMelt, three of the four water content estimates require less than 15 wt ppm H_2O to explain the observed conductivity. Only the colder geotherm and YM+pZY mixture yield hydration values within the range expected from MORB samples (50-200 wt ppm H_2O). The NOMan results are similar to NoMelt below 100 km depth since all of the water content estimates are also lower than the H_2O storage capacity. The WK+pDK estimates suggest the asthenosphere is effectively dry (<20 wt ppm H_2O) while the YM+pZY estimates are in line with MORB inferred values.

The low hydration estimates are atypical and become problematic when the rheological properties of the upper mantle are taken into account. The primary impetus for the competing interpretations of hydration versus partial

melt is that either mechanism has the potential to generate the large viscosity reduction required across the LAB. Since water in olivine is typically assumed to be the primary control on the rheology of hydrated peridotite (Hirth and Kohlstedt, 1996), then a bulk mantle water content of 20 wt ppm H_2O is equivalent to 2.5–7.9 wt ppm H_2O in olivine at depths of 40–200 km. Such a low concentration of water in olivine is possibly insufficient to weaken the asthenosphere to the extent required by geophysical observations and geodynamic models (Karato and Jung, 1998; Kawakatsu and Utada, 2017; Becker, 2017).

6. Conclusions

The electrical conductivity signature of the mantle is sensitive to temperature, composition, hydration, and the presence of partial melt. Considering the range of hydrous olivine conductivity models to choose from, it is difficult to distinguish between hydration and partial melt as the cause of highly conductive mantle. In this study, I have demonstrated that when the thermodynamic stability of hydrous mantle and the role of pyroxenes are taken into account, some of the marine MT observations – beneath young seafloor in particular – require partial melt regardless of which conductivity model is applied. Furthermore, the hydration estimates beneath older seafloor imply that the WK+pDK models are anomalously conductive and may require too little water to explain the relatively low viscosity in the asthenosphere, while the YM+pZY model estimates are within the range of MORB values. If the WK+pDK predictions are indeed accurate, then either water has a much more significant effect on mantle rheology than currently thought or inter-

connected partial melts become a necessity to accommodate the viscosity reduction across the LAB.

Acknowledgements

I would like to thank Elizabeth Ferriss, Derrick Hasterok, Kerry Key, and Anne Pommier for discussions and comments. Kiyoshi Baba, Rob L. Evans, and Emily Sarafian are thanked for providing their magnetotelluric inversion models. Two anonymous referees and the editor are thanked for their constructive reviews that significantly improved the manuscript. This work was supported by a Lamont-Doherty Earth Observatory postdoctoral fellowship. Matlab scripts are available upon request.

References

Anderson, D. L., Sammis, C., 1970. Partial melting in the upper mantle. Physics of The Earth and Planetary Interiors 3, 41–50.

Baba, K., Chave, A. D., Evans, R. L., Hirth, G., Mackie, R. L., 2006. Mantle dynamics beneath the East Pacific Rise at 17 °S: Insights from the Mantle Electromagnetic and Tomography (MELT) experiment. Journal of Geophysical Research 111, B02101.

Baba, K., Tada, N., Zhang, L., Liang, P., Shimizu, H., Utada, H., 2013. Is the electrical conductivity of the northwestern Pacific upper mantle normal? Geochemistry Geophysics Geosystems 14, 4969–4979.

Becker, T. W., 2017. Superweak asthenosphere in light of upper mantle seismic anisotropy. Geochemistry Geophysics Geosystems 18, 1986–2003.

544 Beghein, C., Yuan, K., Schmerr, N., Xing, Z., 2014. Changes in Seismic
545 Anisotropy Shed Light on the Nature of the Gutenberg Discontinuity. Sci-
546 ence 343, 1237–1240.

547 Bell, D. R., Rossman, G. R., Maldener, J., Endisch, D., Rauch, F., 2003.
548 Hydroxide in olivine: A quantitative determination of the absolute amount
549 and calibration of the IR spectrum. Journal of Geophysical Research: Solid
550 Earth 108, B22105.

551 Constable, S., 2006. SEO3: A new model of olivine electrical conductivity.
552 Geophysical Journal International 166, 435–437.

553 Dai, L., Karato, S.-i., 2009. Electrical conductivity of orthopyroxene: Im-
554 plications for the water content of the asthenosphere. Proceedings of the
555 Japan Academy, Series B 85, 466–475.

556 Dai, L., Karato, S.-i., 2014. High and highly anisotropic electrical conduc-
557 tivity of the asthenosphere due to hydrogen diffusion in olivine. Earth and
558 Planetary Science Letters 408, 79–86.

559 Dasgupta, R., Mallik, A., Tsuno, K., Withers, A. C., Hirth, G., Hirschmann,
560 M. M., 2013. Carbon-dioxide-rich silicate melt in the Earth's upper mantle.
561 Nature 493, 211–215.

562 Du Frane, W. L., Tyburczy, J. A., 2012. Deuterium-hydrogen exchange in
563 olivine: Implications for point defects and electrical conductivity. Geo-
564 chemistry Geophysics Geosystems 13, Q03004.

565 Evans, R. L., Hirth, G., Baba, K., Forsyth, D., Chave, A., Mackie, R., 2005.

566 Geophysical evidence from the MELT area for compositional controls on
567 oceanic plates. Nature 437, 249–252.

568 Faul, U. H., Jackson, I., 2005. The seismological signature of temperature
569 and grain size variations in the upper mantle. Earth and Planetary Science
570 Letters 234, 119–134.

571 Fischer, K. M., Ford, H., Abt, D., Rychert, C. A., 2010. The lithosphere-
572 asthenosphere boundary. Annual Review of Earth and Planetary Sciences
573 38, 551–575.

574 Forsyth, D., Scheirer, D. S., Webb, S. C., Dorman, L. M., Orcutt, J. A.,
575 Harding, A. J., Blackman, D. K., Morgan, J. P., Detrick, R. S., Shen, Y.,
576 Wolfe, C. J., Canales, J. P., Toomey, D. R., Sheehan, A. F., Solomon,
577 S. C., Wilcock, W., Team, M. S., 1998. Imaging the deep seismic structure
578 beneath a mid-ocean ridge: The MELT experiment. Science 280, 1215–
579 1218.

580 Gardés, E., Gaillard, F., Tarits, P., 2014. Toward a unified hydrous olivine
581 electrical conductivity law. Geochemistry Geophysics Geosystems 15,
582 4984–5000.

583 Hasterok, D., 2013. A heat flow based cooling model for tectonic plates. Earth
584 and Planetary Science Letters 361, 34–43.

585 Hirschmann, M. M., 2000. Mantle solidus: Experimental constraints and the
586 effects of peridotite composition. Geochemistry Geophysics Geosystems 1,
587 2000GC000070.

588 Hirschmann, M. M., Tenner, T., Aubaud, C., Withers, A. C., 2009. Dehydra-
589 tion melting of nominally anhydrous mantle: The primacy of partitioning.
590 Physics of The Earth and Planetary Interiors 176, 54–68.

591 Hirschmann, M. M., 2010. Partial melt in the oceanic low velocity zone.
592 Physics of The Earth and Planetary Interiors 179, 60–71.

593 Hirth, G., Kohlstedt, D., 1996. Water in the oceanic upper mantle: impli-
594 cations for rheology, melt extraction and the evolution of the lithosphere.
595 Earth and Planetary Science Letters 144, 93–108.

596 Holtzman, B. K., 2016. Questions on the existence, persistence, and mechani-
597 cal effects of a very small melt fraction in the asthenosphere. Geochemistry
598 Geophysics Geosystems 17, 470–484.

599 Jones, A. G., Fullea, J., Evans, R. L., Muller, M. R., 2012. Water in cra-
600 tonic lithosphere: Calibrating laboratory-determined models of electrical
601 conductivity of mantle minerals using geophysical and petrological obser-
602 vations. Geochemistry Geophysics Geosystems 13, Q06010.

603 Karato, S.-i., 1990. The role of hydrogen in the electrical conductivity of the
604 upper mantle. Nature 347, 272–273.

605 Karato, S.-i., Jung, H., 1998. Water, partial melting and the origin of the
606 seismic low velocity and high attenuation zone in the upper mantle. Earth
607 and Planetary Science Letters 157, 193–207.

608 Karato, S.-i., 2013. Theory of isotope diffusion in a material with multiple
609 species and its implications for hydrogen-enhanced electrical conductivity
610 in olivine. Physics of The Earth and Planetary Interiors 219, 49–54.

611 Katsura, T., Baba, K., Yoshino, T., Kogiso, T., 2017. Electrical conductivity
612 of the oceanic asthenosphere and its interpretation based on laboratory
613 measurements. Tectonophysics 717, 162–181.

614 Kawakatsu, H., Utada, H., 2017. Seismic and Electrical Signatures of the
615 Lithosphere–Asthenosphere System of the Normal Oceanic Mantle. Annual
616 Review of Earth and Planetary Sciences 45, 139–167.

617 Libowitzky, E., Rossman, G. R., 1996. Principles of quantitative absorbance
618 measurements in anisotropic crystals. Physics and Chemistry of Minerals
619 23, 319–327.

620 Mierdel, K., Keppler, H., Smyth, J. R., Langenhorst, F., 2007. Water solu-
621 bility in aluminous orthopyroxene and the origin of Earth's asthenosphere.
622 Science 315, 364–368.

623 Mosenfelder, J. L., Deligne, N. I., Asimow, P. D., Rossman, G. R., 2006.
624 Hydrogen incorporation in olivine from 2-12 GPa. American Mineralogist
625 91, 285–294.

626 Naif, S., Key, K., Constable, S., Evans, R. L., 2013. Melt-rich channel ob-
627 served at the lithosphere–asthenosphere boundary. Nature 495, 356–359.

628 O'Leary, J. A., Gaetani, G. A., Hauri, E. H., 2010. The effect of tetrahedral
629 Al^{3+} on the partitioning of water between clinopyroxene and silicate melt.
630 Earth and Planetary Science Letters 297, 111–120.

631 Paterson, M. S., 1982. The determination of hydroxyl by infrared absorption
632 in quartz, silicate glasses and similar materials. Bulletin de Mineralogie
633 105, 20–29.

Poe, B. T., Romano, C., Nestola, F., Smyth, J. R., 2010. Electrical conductivity anisotropy of dry and hydrous olivine at 8 GPa. Physics of The Earth and Planetary Interiors 181, 103–111.

Saal, A. E., Hauri, E., Langmuir, C. H., Perfit, M. R., 2002. Vapour undersaturation in primitive mid-ocean-ridge basalt and the volatile content of Earth's upper mantle. Nature 419, 451–455.

Sarafian, E., Evans, R. L., Collins, J. A., Elsenbeck, J., Gaetani, G. A., Gaherty, J. B., Hirth, G., Lizarralde, D., 2015. The electrical structure of the central Pacific upper mantle constrained by the NoMelt experiment. Geochemistry Geophysics Geosystems 16, 1115–1132.

Sarafian, E., Gaetani, G. A., Hauri, E. H., Sarafian, A. R., 2017. Experimental constraints on the damp peridotite solidus and oceanic mantle potential temperature. Science 355, 942–945.

Schock, R. N., Duba, A. G., Shankland, T. J., 1989. Electrical conduction in olivine. Journal of Geophysical Research 94, 5829–5839.

Sifré, D., Gardés, E., Massuyeau, M., Hashim, L., Hier-Majumder, S., Gaillard, F., 2014. Electrical conductivity during incipient melting in the oceanic low-velocity zone. Nature 509, 81–85.

Stein, C. A., Stein, S., 1992. A model for the global variation in oceanic depth and heat flow with lithospheric age. Nature 359, 123–129.

Stixrude, L., Lithgow-Bertelloni, C., 2005. Mineralogy and elasticity of the oceanic upper mantle: Origin of the low-velocity zone. Journal of Geophysical Research 110, B03204.

Wang, D., Mookherjee, M., Xu, Y., Karato, S.-i., 2006. The effect of water on the electrical conductivity of olivine. Nature 443, 977–980.

Withers, A. C., Bureau, H., Raepsaet, C., Hirschmann, M. M., 2012. Calibration of infrared spectroscopy by elastic recoil detection analysis of H in synthetic olivine. Chemical Geology 334, 92–98.

Xu, Y., Shankland, T. J., 1999. Electrical conductivity of orthopyroxene and its high pressure phases. Geophysical Research Letters 26, 2645–2648.

Yang, X., 2012. Orientation-related electrical conductivity of hydrous olivine, clinopyroxene and plagioclase and implications for the structure of the lower continental crust and uppermost mantle. Earth and Planetary Science Letters 317–318, 241–250.

Yoshino, T., Matsuzaki, T., Yamashita, S., Katsura, T., 2006. Hydrous olivine unable to account for conductivity anomaly at the top of the asthenosphere. Nature 443, 973–976.

Yoshino, T., Matsuzaki, T., Shatskiy, A., Katsura, T., 2009. The effect of water on the electrical conductivity of olivine aggregates and its implications for the electrical structure of the upper mantle. Earth and Planetary Science Letters 288, 291–300.

Yoshino, T., Katsura, T., 2013. Electrical Conductivity of Mantle Minerals: Role of Water in Conductivity Anomalies. Annual Review of Earth and Planetary Sciences 41, 605–628.

Zhang, B., Yoshino, T., Wu, X., Matsuzaki, T., Shan, S., Katsura, T., 2012.

679 Electrical conductivity of enstatite as a function of water content: Implica-
680 tions for the electrical structure in the upper mantle. Earth and Planetary
681 Science Letters 357–358, 11–20.

682 Zhao, C., Yoshino, T., 2013. Electrical conductivity of mantle clinopyroxene
683 as a function of water content and its implication on electrical structure
684 of uppermost mantle. Earth and Planetary Science Letters 447, 1–9.